Path Planning for a Circular Parachute Using Descent Rate Control

Travis D. Fields,* Jeffrey C. LaCombe†
and Eric L. Wang‡

University of Nevada, Reno, Nevada, 89557, USA

This paper presents a time-varying control methodology for a variable-sized circular parachute to reach a target landing location. A trajectory is calculated for the immediate control horizon using wind forecast data. In order to create a parachute–payload trajectory, a 3–DOF kinematic model is developed. Using this, the performance envelope is determined, revealing the potential target range of the system throughout a descent. Next, this model is extended to develop a control methodology to determine the descent rate, via parachute size manipulation, needed to reach the desired landing target. Finally, simulation results are presented to validate the control scheme. Various release locations were simulated with paired uncontrolled/controlled parachute descents from within the performance envelope. Results demonstrate the feasibility of the system, with controlled parachute descents navigating towards the target. With accurate wind data the vehicle can overcome release location errors as well as vehicle uncertainties and perform significantly better than an uncontrolled parachute.

Nomenclature

A	=	Parachute reference area (A_{max} = maximum, A_{min} = minimum, A_{nom} = average of A_{min} and A_{max})
$\vec{B}_i$	=	Current probe direction unit vector
C_d	=	Coefficient of drag
f	=	Drag area, $C_d A$. (f_{ij} = drag area for current probe direction i and wind layer j, $f_{d,n}$ is the desired drag area in layer n, f_{min} and f_{max} are the minimum and maximum achievable drag configurations.)
F_d	=	Vertical parachute induced drag
F_g	=	Gravitation force resulting from gravitational acceleration g
h	=	Altitude used in calculation of performance envelope
i	=	Subscript used for controlled descent algorithm as the current probe direction index
j	=	Subscript used for current altitude index in constructing the performance envelop construction (measured bottom-up)
m	=	Total mass of combined parachute–payload system
N	=	Number of layers in the performance envelope
n	=	Subscript used for current altitude index in the controlled descent algorithm (measured top-down)
$\vec{w}_n$	=	Current wind velocity vector at altitude/time step n, ($w_{x,n}$ and $w_{y,n}$ are horizontal components in east/west and north/south directions)
x_c, y_c	=	east/west and north/south coordinates of the performance envelope centroid

---

*Graduate Research Assistant, Mechanical Engineering, 1664 N Virginia St. MS 312, Reno, NV, and AIAA Member.
†Associate Professor, Chemical and Materials Engineering, 1664 N Virginia St. MS 388, Reno, NV, and AIAA Member.
‡Associate Professor, Mechanical Engineering, 1664 N Virginia St. MS 312, Reno, NV.

American Institute of Aeronautics and Astronautics

x_n, y_n	=	Calculated horizontal predicted position coordinates at the nth time step. For example,
		$x_{d,n}$ = desired displacement in east/west direction in layer n,
		$x_{min,n}$ and $x_{max,n}$ are the minimum and maximum displacements,
		$\hat{\dot{x}}_n$ is the estimated horizontal velocity in the east/west direction,
		$\ddot{x}$ is the estimated horizontal acceleration in the east/west direction
z_n	=	Calculated predicted vertical position coordinates at the nth time step. For example,
		Δz is the change in vertical position over a given time step (positive = descending)
		$\hat{z}_n^{TV}$ is the vertical position at time step n, assuming terminal velocity (zero acceleration)
		$\dot{z}$ is the vertical component of velocity,
		$\ddot{z}$ is the vertical component of acceleration
Δh	=	Change in vertical position over a given time step with a positive result when ascending
Δt	=	Time step. Δt_{ij} is the time step for current probe direction i, in layer j
$\delta_{d,n}$	=	Minimum horizontal distance from current location to parachute area transition line along the current wind direction
$\rho(z)$	=	Air density as a function of altitude z
λ	=	Desired scaling between maximum and minimum parachute size

I.   Introduction

Over the past 15 years, there has been considerable effort in developing accurate autonomous descent vehicles (ADVs) for use in payload delivery. An early concept used a deformable circular parachute actuated via pneumatics.[1,2,3] This method provided rudimentary horizontal steering by simply straining the suspension lines. The canopy deformation resulted in glide slopes of up to 0.5. Due to the large mass of the system (from the need for large amounts of compressed nitrogen gas), other more feasible options were pursued, including electromechanically–deformed parachutes.[4,5]

A second ADV method involved the use of maneuverable ram–air parafoils. These parafoils have achieved significantly higher glide slopes as well as wind–based error rejection[6,7,8] when compared to the deformable circular parachute systems. Using small brake deflections, the vehicle is able to directly control the direction of horizontal motion. Recently, glide slope control has also been achieved using both spoilers and simultaneous brake deflection.[9] This system requires a complex model to accurately predict the motion of the vehicle during descent.

The above–mentioned precision airdrop systems require hardware modifications (or entire hardware replacements) to existing airdrop systems. This disadvantage[10] could hinder precision airdrop implementation in situations with lower priority as both time for training and monetary funds may not be readily available for uses such as humanitarian relief airdrops. A path-planning prediction system has been developed for use with standard uncontrolled military circular parachutes.[11] A similar guided system that uses path planning has been developed based on a standard circular parachute with minimal changes to the existing drop system hardware.

This approach exerts limited but useful control over the landing location by reversibly reefing the canopy.[12] Using accurate wind data, the ADV modifies its descent velocity to control the distance traveled downwind. The control system assumes the vehicle makes only a single actuation for the remaining portion of the descent (i.e., the drag area remains constant). To reduce wind–induced landing location errors, the system periodically adjusts the canopy size, and thus, the descent velocity. Consequently, the landing location is constrained to lie on a line segment along the prevailing wind direction as opposed to a single target point.

As an extension to this constant drag area methodology, the present work incorporates multiple parachute drag area changes in the operation scheme. This extension greatly increases the controllability of the system, and enables reaching a desired target point. By using multiple actuations, the system can increase the descent rate to spend less time in winds that push away from the target point, and when subjected to winds that push towards the target point, the system can decrease the descent rate to fully exploit favorable wind layers. This method has potential use in high altitude airdrops, as the larger the atmospheric column, the more maneuverability the vehicle will possess. There are also potential applications in guiding payloads to surface

American Institute of Aeronautics and Astronautics

targets from planetary orbits (Mars, for example).[13]

Currently, high altitude low opening (HALO) airdrops provide the highest accuracy in high altitude airdrop systems. As with any circular parachute drop, the accuracy of this technique is vulnerable to release location errors. The descent rate control methodology described herein mitigates these errors, while still presenting a high altitude capable system. Additionally, as the vehicle controls its descent rate directly, it can correct for vehicle uncertainties (e.g. payload mass and parachute/payload drag area). If the vehicle is not falling fast enough (based on the desired trajectory), then it simply reefs the parachute more until the desired velocity is reached.

The descent rate control methodology described herein provides a stepping stone in implementing descent rate control for other autonomous decent vehicles and aircraft. Planning descent trajectories using descent rate control can improve landing accuracy, and help minimize the control system energy necessary to reach the target.

Because horizontal motions of this system are solely dependent on the wind (actuations modify descent rate only), foreknowledge of the wind is crucial. The quality of the wind data gathered can be categorized into three distinct categories: Type A, Type B, and Transition type wind data. Type A wind data is collected (or forecasted) with large spatial and/or temporal differences from that of the actual wind seen during vehicle descent. Type B wind data is collected in the immediate region of the anticipated vehicle descent both spatially and temporally. The resulting predicted wind data then contains relatively small-scale errors. Transition type wind data exhibits some aspects of both Type A and B wind data errors. It is usually collected in the vicinity of the anticipated release and within 30 minutes of the anticipated release. The more accurate (Type B) wind data can be collected (for example) using dropsondes or radiosondes.[14,15,16]

Central to the descent rate control methodology is a means by which the descent rate can be altered. A reversible reefing method was developed for the test system in this study, using a mechanical reeling system to wind the parachute shroud lines in and out. This causes the canopy size to increase or decrease, and the descent rate of the vehicle can be controlled. Descent rate field testing has been performed using several parachute designs, with best results obtained with a quarter-spherical cross-based canopy (Figure 1). Tests have shown that the parachute can be reliably reefed from a parachute drag area of $4.5m^2$ down to $1.3m^2$. For a payload mass on the order of 5kg, this represents a descent speed range of $\approx 5m/s$ in the fully open configuration, and up to $\approx 10m/s$ in the fully-reefed configuration. In these tests, the four suspension line quarter-spherical cross design posed no shroud line tangling problems and resisted collapsing completely when reefed in significantly (without a spreader ring), compared to other traditional slotted spherical parachutes tested. The maximum amount of reefing possible is limited due to concerns over the canopy getting reeled into the mechanism, causing jams that would prevent the parachute from reeling back out. In order for the reeling mechanism to draw the parachute lines in, the reeling mechanism must be capable of lifting the payload weight. This is easily implemented for small scale vehicles; however, for heavier payloads, alternative reversible reefing techniques may be necessary. It is important to note the reefing method described is simply a proof-of-concept, and other more feasible approaches of modifying the parachute/payload descent speed may exist.
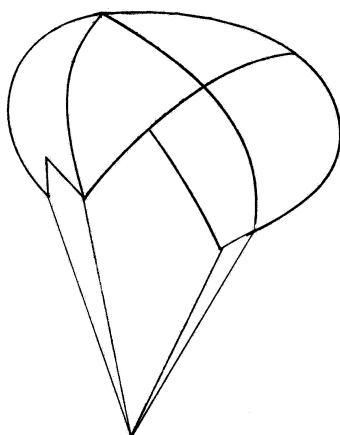
Figure 1. Quarter-spherical cross–based canopy used in this study. Similar to canopies used in automotive drag racing.

American Institute of Aeronautics and Astronautics

Another benefit of the reefing method described is its inherit ability to manage canopy inflation loads, accomplished by simply deploying the vehicle in the fully-reefed configuration. After steady state has been reached, the vehicle can de-reef as necessary to reach the desired descent speed.

II.   Parachute–Payload Descent Model Development

In this section, the development of a three degree–of–freedom parachute–payload model is presented. The following assumptions are made:

- Parachute vertical drag is significantly greater than payload drag.

- Rotational motion of the parachute–payload system negligibly affects the translational and vertical motion of the system.

- Lateral drag forces and inertial effects in the system are negligible, and the system moves with the wind laterally at all times.

- The vertical component of the wind, w_z, is typically small compared to the descending velocity.[17]

- Internal forces between the parachute and payload are neglected as the actuator and suspension lines are capable of providing/handling the forces required to reef the canopy.

- Changes to the system configuration occur instantaneously.

As the system is not rotating, the equations of motion are defined in the inertial frame. Following these assumptions, the system can be simplified to a single rigid body with parachute area A, and system mass m. For convenience, the derivations of the equations of motion have been decoupled into horizontal and vertical components.

The operating scheme is based on the notion that by manipulating the parachute size, the descent rate can be modified, thereby affecting the landing location of the ADV. The system uses the varying winds throughout the air column by deliberately changing the amount of time spent descending through each layer. By determining and configuring for the optimal parachute size in each wind layer, we establish time–varying control that enables the vehicle to effectively steer towards the target landing location. Optimality for this work has been defined as the solution which minimizes the distance from a desired landing location, and is not associated with any form of optimal control strategy. If the wind in a given layer contributes constructively towards the desired trajectory, the parachute opens to maximize the benefits of the constructive wind. Conversely, if the drift direction is counterproductive, the parachute is closed (reefed), minimizing the amount of time spent in that layer. In the event of vertical winds or vehicle uncertainties, the descent vehicle can overcome the induced descent speed error by reefing (or de-reefing) the parachute (limited by the maximum or minimum reefing values).

A.   Vertical Motion

The equation of motion in the vertical direction is expressed in terms of gravitational and drag forces acting on the parachute–payload system. This is written as

$$m\ddot{z} = F_d - F_g. \tag{1}$$

In Equation (1), the gravitational force is the conventional $F_g = mg$ and the drag force is assumed to be solely in the vertical direction, and of the form

$$F_d = \frac{1}{2}\rho\left(z\right)AC_d\dot{z}^2. \tag{2}$$

Equations (1) and (2) combine to yield

$$\ddot{z} = \frac{\rho\left(z\right)AC_d\dot{z}^2}{2m} - g. \tag{3}$$

It is important to note that the density cannot be assumed constant, and therefore a closed-form solution to $z(t)$ using Equation (3) is not readily expressed. However, using standard atmospheric data tables[18] or

American Institute of Aeronautics and Astronautics

directly measured density data, Equation (3) can be solved numerically using a suitable numerical integration routine to produce altitude as a function of time, $\hat{z}(t)$ during descent.

Although the numerical integration provides an accurate numerical estimation of the altitude over time, $\hat{z}(t)$, a more computationally–efficient method results from assuming the vehicle is at terminal velocity at all times. The descent rate at each time step can then simply be calculated using Equation (3) with the constraint that $\ddot{z} = 0$, assuming the descent occurs quasistatically, and the vehicle does not accelerate during each time step (requires a sufficiently-small time step). The significance of this simplification will become evident in the controller development section of this paper. Note though, that the terminal velocity will vary slowly between time steps, due to variations in air density with altitude and changes in the drag area.

$$\dot{z}_n = -\sqrt{\frac{2mg}{\rho(z_n)AC_d}} \tag{4}$$

Here the index n is used to denote a descent trajectory layer (top-down). In order to calculate the entire predicted descent profile, $\hat{z}^{TV}(t)$, the terminal velocity must be calculated at each time step using the corresponding air density. Once this descent rate is calculated for a particular time step, the change in altitude can be determined by using the zero–acceleration kinematics equation:

$$\hat{z}_n = \hat{z}_{n-1} + \dot{z}_n \Delta t_n \tag{5}$$

For a uniform step size in altitude ($\Delta z = z_n - z_{n-1}$), this equation can be rearranged and combined with Equation 4 to yield

$$\Delta t_n = -\frac{\Delta z}{\sqrt{\frac{2mg}{\rho(z_n)AC_d}}} \tag{6}$$

The terminal velocity assumption was verified by comparing simulations performed using both the numerical integration of Equation 3 and an implementation of the terminal velocity expression in Equations 4–6. Figure 2 shows the descent rate as a function of time for both the numerical integration and the simpler terminal velocity simulations. The release altitude was selected as 9.1km MSL (30,000ft), with a landing target altitude of 0.0km MSL. Integration time steps used were 1 sec. Convergence between the two methods is clearly seen within the first four seconds of the simulation. For lower release altitudes, the convergence is faster; for example, a release from 2.0km (6,500ft) reaches terminal velocity in approximately two seconds. The terminal velocity approximation approaches the full numerical integration simulation, although in practice, both predictive techniques can differ from the actual performance due to modeling uncertainties such as inaccurate C_d values, etc. From the comparison in Figure 2, it is concluded that the terminal velocity approach is sufficiently accurate, and because of its simplicity, can be used for all descent prediction profile calculations.

B.   Horizontal Motion

Once the vertical motion is estimated for the remainder of a descent, the time to be spent at each altitude is known. Using this, along with a predicted wind data set, the horizontal motion can be calculated. As discussed previously, horizontal motion is purely governed by the wind, and can be calculated using the zero-acceleration kinematics equations:
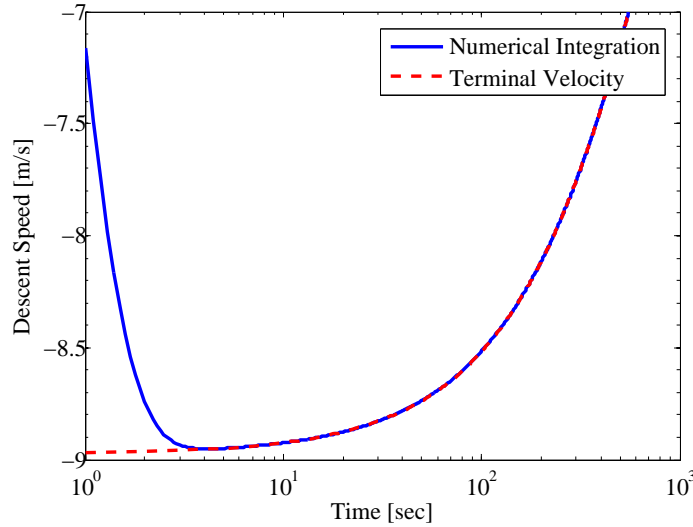
$$x_n = x_{n-1} + \hat{\dot{x}}_n \Delta t_n \tag{7}$$

$$y_n = y_{n-1} + \hat{\dot{y}}_n \Delta t_n \tag{8}$$

Where it is assumed that the parachute–payload system travels at the wind speed, w, yielding:

$$x_n = x_{n-1} + w_{x,n} \Delta t_n \tag{9}$$

$$y_n = y_{n-1} + w_{y,n} \Delta t_n \tag{10}$$

American Institute of Aeronautics and Astronautics

Figure 2. Calculated velocities during a descent using both the full numerical integration and the terminal velocity simulations.

In order for Equations 9 & 10 to accurately predict the horizontal motion, the parachute–payload system must reach the wind speed sufficiently quickly, and Δt should be sufficiently small. Corrections for this inertia–induced wind measurement error have been previously developed.[16] The correction terms were derived by incorporating the inertial effects. Simplifications were made by assuming the vehicle descent velocity is much greater than the horizontal velocity error (horizontal velocity relative to the wind) resulting in Eqs. 11 & 12. With horizontal accelerations typically below $0.5 m/s^2$ and descent velocities up to $9 m/s$, correction factors will be less than $0.5 m/s$ (typically less than $0.3 m/s$) which is at or below the correction factors accuracy of $\pm 0.5 m/s$. In order to simplify computations of raw data, these correction factors are not used as they are typically within the equations published accuracy.

$$w_{x,n} \approx \dot{x}_n - \frac{\ddot{x}_n \dot{z}_n}{g} \tag{11}$$

$$w_{y,n} \approx \dot{y}_n - \frac{\ddot{y}_n \dot{z}_n}{g} \tag{12}$$

III.   Performance Envelope

The first step in development of the present control scheme is to determine the so-called performance envelope of the descent rate controlled parachute and payload system. The envelope encompasses the set of all points from which the target can be reached during a controlled descent. This envelope can be envisioned as a horn–shaped volume extending upwards and upwind from the target location on the ground.

The performance envelope is determined using given wind conditions and is calculated for a single bearing direction at a time (the probe direction, $\vec{B}_i$). Within each control layer, the descent rate is configured to maximize the horizontal drift vector's component along the probe direction. If the wind is counter to the probe direction, then control in the simulation is exerted to minimize its influence. The net drift over all N layers is then totaled as the maximum possible drift in that bearing direction. By repeating the process for all bearing directions, the bounding envelope can be calculated without wasting computation time on identifying internal points. This method generates a set of points that all fall precisely on the bounding surface of the performance envelope—avoiding the inefficiency of approaches that track all possible motions and map those that reach the target to estimate the envelope. With minor adjustments, this efficient method for performance envelope calculation can be implemented in path planning schemes for other types of descent vehicles. A more detailed description of this boundary probing simulation is presented here.

For convenience, the target location is set to $(x_t, y_t, z_t) = (0, 0, z_t)$. The bounding envelope calculation starts at the target location and works upward (backward) through the N wind layers, each of thickness

American Institute of Aeronautics and Astronautics

$\Delta h = h_j - h_{j-1}$, to the release altitude. The envelope's horizontal cross section shape is calculated in this manner at a given altitude using the wind prediction data. This process is then repeated to find the subsequent envelope for the next altitude layer. For this derivation, it is assumed the wind prediction data is sorted in ascending order ($j = N - n$) where $h_{N-j} = z_n$. The change in time between two successive layers is

$$\Delta t_{ij} = -\frac{\Delta h}{\sqrt{\frac{2mg}{\rho_j f_{ij}}}} \tag{13}$$

Here, f_{ij} is the parachute drag area, and is dependent on both the current probe direction i, and layer j. In order to calculate the largest possible boundary envelope, only the maximum and minimum possible drag areas are considered (zero or full reefing):

$$f_{ij} = \begin{cases} C_d A_{max} : \vec{B}_i \cdot (-\vec{w}_j) > 0 \\ C_d A_{min} : \vec{B}_i \cdot (-\vec{w}_j) < 0 \end{cases}$$

Note that within a given layer j, Δt_{ij} will vary and take one of two distinct values, depending on the angle between the wind and probe directions. Additionally, between layers, Δt_{ij} will also vary due to air density changes. Lastly, it is important to note that Δt_{ij} will always be negative as Δh is positive when constructing from the ground up. This causes the horizontal displacements (Equations 9 & 10) to be in the opposite direction to the wind, which makes intuitive sense, as the envelope is constructed ground–up (backwards in time). For the special case when the wind in a layer is zero ($\vec{w}_j = \mathbf{0}$), the previous (below) drag area is maintained.

With the above mathematical construction, a favorable wind condition exists in an individual layer when $-\vec{w}_j$ is within $\pm 90°$ of the current probe direction ($\vec{B}_i$). In such a case, the maximum drag area is used to slow the ADV's descent within this layer, and take maximum advantage of the favorable wind.

An example of the boundary envelope construction is depicted in Figure 3. For this example, the performance envelope is calculated using eight probe directions (simplified for the purpose of demonstration). The procedure starts at the ground layer ($j = 0$) by initializing the envelope to the origin (target point). In this layer, the envelope consists of a single point at $(0, 0)$, with the 8 probe directions shown by their respective arrows. The next layer ($j = 1$) incorporates the first decision making process in which each probe direction is compared with the layer's wind direction (depicted by the vector plotted in the center). Positions that resulted from control decisions to select the maximum drag area are plotted with a ×, while decisions to use the minimum drag area are plotted with a ∘.

The envelope for the first layer (above the ground) takes the form of a line connecting the two distinct boundary points resulting from consideration of the 8 probe directions. Note that in this first layer, there can be only two possible new positions (resulting from either maximum or minimum drag area), thus the 8 different probe directions are grouped into two coincident clusters at each end of the line segment. The second layer ($j = 2$) further unfolds the performance envelope into a two-dimensional shape. As the wind has changed direction significantly from $142°$ in layer 1 to $19.9°$ in layer 2, different drag areas are selected in comparison to the previous layer. Probe directions 8, 1, and 2 all favored the maximum drag area configuration for layer 1, but chose the minimum drag area for layer 2. Extending the illustration with one more layer ($j = 3$), it is seen that it is possible to have fewer unique boundary points than the maximum (2^j).

Note that the farthest distances achievable when probing both the B_1 and B_2 directions result at the same point. This illustrates that for a finite number of wind layers (and control actuations), it is not possible to generate a continuous set of points defining the boundary envelope. Instead, this construction method makes a "best attempt" to evaluate lateral motion in a given probe direction, and will guide the parachute as close to that direction as is possible, given the finite number of control actuations. In general, the maximum number of unique boundary points increases as 2^j, up to the number of probing directions selected (360 for this study).

The process of constructing the horizontal displacement for each layer is generally repeated through all N layers up to the release altitude at layer $j = N$. An example of a cross section from an envelope using 360 probe directions and wind data collected from a balloon (Figure 4) is shown in Figure 5. Here, the envelope is constructed at the 500th layer ($j = 500$) at an altitude of $9km$. If the predicted wind data is very accurate, the target location can be reached by any release point that lies within or on the boundary
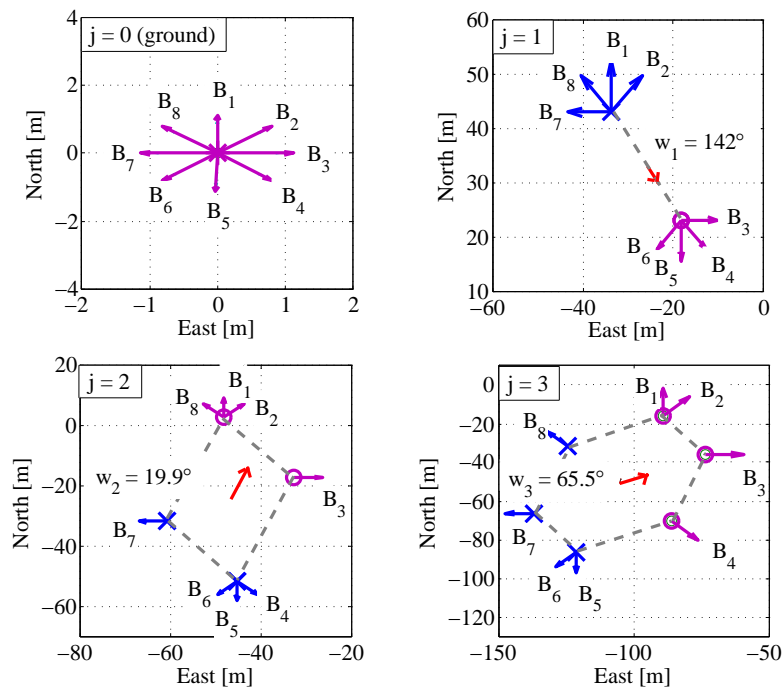
Figure 3. First four steps of the performance envelope construction process.

of the performance envelope. Once the envelope has been fully constructed (Figure 6), the ideal calculated aerial release point (CARP) can be determined.
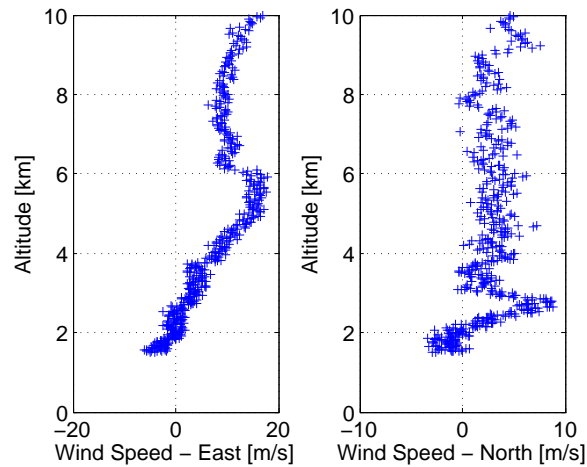

Figure 4. Wind profile collected from a balloon and used to generate the performance envelope.

IV.   Control Methodology

The control approach developed here consists of a series of single–actuation choices. This is because for a given change in altitude, the parachute–payload system can only influence the time spent in that layer and the distance traveled downwind. By making a series of choices (with varying wind directions in each layer), the system can effectively control translation in two dimensions (latitude and longitude).

A robust control scheme is developed in which the system attempts to travel towards the center of the performance envelope, maintaining maximum flexibility for future decisions. For this work, robustness is
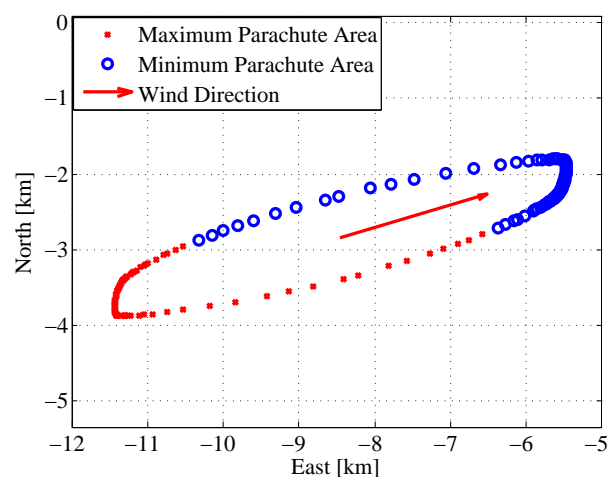
American Institute of Aeronautics and Astronautics

Figure 5. Single layer from the performance envelope using 360 probe directions.
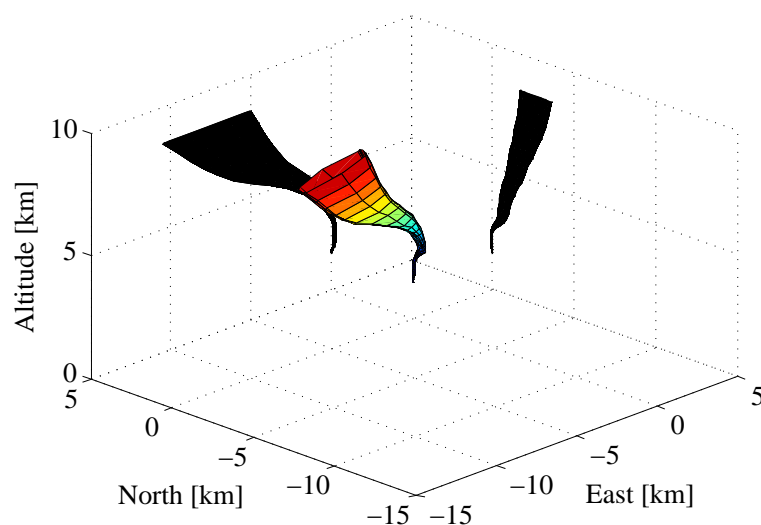

Figure 6. Full performance envelope calculated using 360 probe directions.

defined as the location providing the largest perturbation rejection in any single direction (located at the center of the performance envelope), and is not associated with a form of conventional robust control strategy. Once at the center, this location provides the maximum degree of control authority to correct for inaccurate wind data. If the wind data is completely accurate, once at the center of the performance envelop, no further changes to the parachute would be needed to reach the target point. This configuration would result in a descent speed that is the average of the maximum and minimum achievable descent speeds at each altitude. Inaccurate wind data will cause the descent vehicle to stray from the center of the performance envelope, prompting the control system to make adjustments to the drag area.

In order to reach the center of the performance envelop, it might be (mistakenly) postulated that it is desirable to travel towards a line that is both normal to the wind vector and passes through the centroid of the performance envelop (dashed line in Figure 7). Once on the dashed line, the wind can neither help nor hinder progress towards the center within that layer. However, attempting to reach this line can easily result in exiting the performance envelope, rendering the system incapable of reaching the desired target. This is illustrated in Figure 7. Starting at the point labeled "current position," the dashed line lies upwind.

American Institute of Aeronautics and Astronautics

To avoid being pushed farther from the dashed line (downwind), the vehicle needs to spend as little time as possible in such unfavorable winds, and would configure to minimize the drag area (descending through the unfavorable wind layer quickly). However, as all the boundary points in the vicinity of the "current position" were generated using a maximum drag area, working towards the dashed line can cause the vehicle to drift towards the boundary (while approaching the dashed line) and actually exit the performance envelope. Once outside of the performance envelope in any wind layer, it is no longer possible to reach the target on the ground.
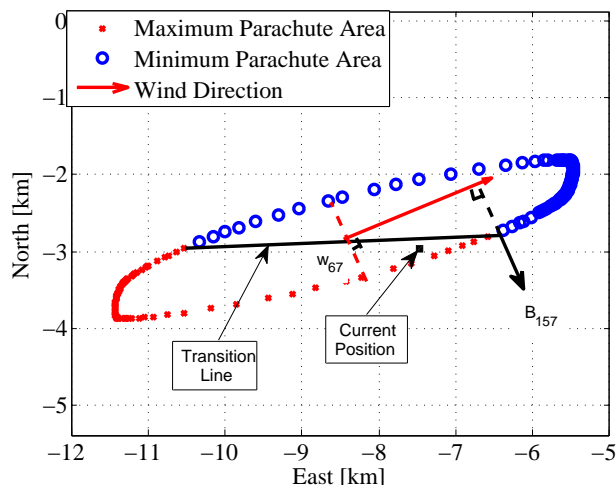
Figure 7. Single layer from performance envelope generated using 360 probe directions. Transition line connects boundary points that transition between maximum and minimum drag area.

To develop an algorithm to efficiently reach the center of the envelope, it is helpful to define a transition line that divides the envelope into two decision-making regimes: locations that require a fast descent rate, and locations that require a slow descent rate. Visually, the envelope is bisected by the transition line (Figure 7). The transition line is most easily constructed by identifying and connecting the two points along the perimeter of the envelope whose surface normals are perpendicular to the wind vector. The transition line always passes through the centroid of the performance envelope. This is due to the inherent binary nature of the envelope construction process that produces a closed shape with an apparent 180 degree rotational symmetry. All points upwind of the transition line require canopy configurations that slow the descent in order to spend more time benefiting from the upwind conditions. Whereas, all points downwind of the transition line correspond to canopy configurations that speed the descent to minimize the time spent being carried downwind.

If the parachute-payload system is on the transition line but not at the centroid, the system must wait (as it continues to descend) for a shift in wind direction that permits further progress towards the centroid. Thus, the transition line directly determines the closest achievable distance to the centroid for a given layer. Returning to the previous example, the transition line lies downwind of the black square (current position) (Figure 7), and, thus, the vehicle will choose to maximize the drag area, moving the vehicle move away from the boundary, closer to the transition line. With this in mind, the goal of the control system is to adjust the drag area so that the vehicle ends up on the transition line. Because the transition line is a linear target, the control methodology previously developed[12] can be used at each altitude to approach the transition line.

The amount of reefing required is proportional to the distance, $\delta_{d,n}$, from the current position to the transition line projected along the current wind direction vector, $\vec{w}_n$. The control system estimates the needed reefing by first estimating the necessary displacement for the vehicle to translate to the transition line in the current layer (or at least make the most progress possible within the layer). This desired displacement has the form:[12]

$$\delta_{d,n} = \sqrt{x_{d,n}^2 + y_{d,n}^2} \tag{14}$$

American Institute of Aeronautics and Astronautics

Where,

$$x_{d,n} = \lambda_n \left(x_{max,n} - x_{min,n} \right) + x_{min,n} \tag{15}$$

$$y_{d,n} = \lambda_n \left(y_{max,n} - y_{min,n} \right) + y_{min,n} \tag{16}$$

The parameter λ_n ranges from $0 \rightarrow 1$ and represents the extent of reefing between the maximum and minimum drag areas, $f_{min} \rightarrow f_{max}$. It is estimated by considering the controllable range of reachable locations, represented graphically as a line of positions between $(x_{min,n}, y_{min,n})$ and $(x_{max,n}, y_{max,n})$. This is compared with the transition line of Figure 7, which spans the envelope between (x_{t1}, y_{t1}) and (x_{t2}, y_{t2}). The intersection point of these two lines yields the desired λ_n:

$$\lambda_n = \frac{(x_{min,n} - x_{t1,n})(y_{t1,n} - y_{t2,n}) + (y_{min,n} - y_{t1,n})(x_{t2,n} - x_{t1,n})}{(x_{t2,n} - x_{t1,n})(y_{min,n} - y_{max,n}) - (x_{min,n} - x_{max,n})(y_{t2,n} - y_{t1,n})} \tag{17}$$

A quadratic interpolation scheme is employed to estimate the desired drag area setting using the maximum, minimum, and nominal drag areas:

$$f_{d,n} = A_{min} + \frac{A_{nom} - A_{min}}{\delta_{nom,n} - \delta_{min,n}} (\delta_{d,n} - \delta_{min,n}) + \frac{\frac{A_{max} - A_{nom}}{\delta_{max,n} - \delta_{nom,n}} - \frac{A_{nom} - A_{min}}{\delta_{nom,n} - \delta_{min,n}}}{\delta_{max,n} - \delta_{min,n}} (\delta_{d,n} - \delta_{min,n})(\delta_{d,n} - \delta_{nom,n}) \tag{18}$$

In each layer during the descent, Equation 18 provides the desired drag area that results in the vehicle reaching the transition line in the minimum amount of time (although it may require more than one layer). The process is then repeated during the descent to continually seek the center point of the performance envelope. This algorithm requires the performance envelope to be known (which can be estimated before hand as long as winds are known). During the descent, though, the control algorithm only looks ahead one layer at a time (minimum control horizon). Using the reference trajectory from the performance envelope calculations, this presents a computationally efficient algorithm which can be easily implemented on a small microprocessor included in the flight hardware.

The center of the performance envelope also has the benefit of falling along the minimum actuation path. This is because the center of the performance envelope is the single actuation case with the average descent velocity achievable in the current configuration. If the vehicle is off of this minimum energy trajectory, the vehicle will navigate towards the center of the envelope. Once at the center, it will require no further actuation (assuming perfectly-known wind data).

V. Simulation Description

With the control approach employed here, the main challenges are envisioned to come from imperfect knowledge of the wind speeds and directions throughout the air column. For many geographical areas, wind data is periodically measured at various locations using sounding balloons (radiosondes) or acoustic soundings (echosondes). However, use of such data can be detrimentally inaccurate if the descent vehicle is deployed at a different time and/or location than the wind data was collected or if natural variations in the wind become significant (gusts, etc.). Inaccurate wind data will result in improper parachute trim commands being issued by the control algorithm. An alternative is to make direct measurements of the wind field immediately prior to deployment of the descent vehicle using a sounding balloon or a suitable dropsonde, deployed from an aircraft.[14]

To determine the impact of inaccurate wind data on the performance of the system, three types of errors in the wind data were investigated using simulations: 1) Type A errors caused by large spatial and/or temporal differences between the predicted and actually-experienced winds, 2) Type B errors caused by measurement precision limitations, inaccuracies, and/or small-scale variations in the wind, and 3) Transition wind errors in which the predicted wind data exhibits characteristics of both Type A and B errors. For all of the results presented, the simulated deployment altitudes were $10km$. Table 1 details the simulation parameters used for the simulations.

American Institute of Aeronautics and Astronautics

Payload Mass	$5.50 kg$
f_{max}	$4.56 m^2$
f_{mid}	$2.50 m^2$
f_{min}	$1.30 m^2$
Release Altitude	$10.0 km$
Landing/Ground Altitude	$1.5 km$
Δh	$5m$

Table 1. Simulation parameters used in all descent simulations.

To investigate these wind errors, simulations were conducted in which the control algorithm made decisions using "inaccurate" wind data for the control decisions, while the vehicle's simulated motion was subjected to "true" wind in the kinematic motion simulation (wind data are discussed more below). Each controlled descent was paired with an uncontrolled descent vehicle, using the middle (f_{mid}) drag area configuration. As described previously, the key benefit of this system is the ability to overcome release location errors. For this reason, release locations were selected throughout the performance envelope (at the release altitude) simulating various release location errors. The number of simulated release locations varied between 21 and 43 depending on the specific wind data sets used. An example of a typical simulation initialization (release points) is shown in Figure 8.
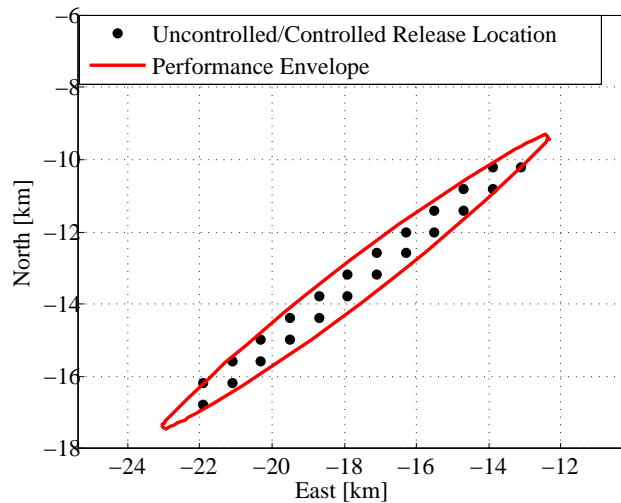
Figure 8. Release locations of simulated uncontrolled and controlled parachute vehicles for a typical descent simulation at a release altitude of 10km.

To provide realistic estimates of performance in the simulations, actual wind data was obtained from numerous field measurements that were paired with each other to represent the "true" and "inaccurate" winds. Fourteen wind data sets were collected with seven gathered from balloon ascents, and seven collected from dropsonde descents (following the balloon ascents). These data sets were obtained during two field tests with four balloons launched simultaneously in the first test group, followed by three more in a second test group approximately one hour later. Dropsondes were released at each balloon burst which varied in time and location for each balloon. Taken together, these 14 wind data sets were mixed and paired to provide a selection of Type A, Type B, and Transition wind error comparisons. The ascent rates of all balloons were matched to each other nearly identically.

VI.   Simulation Results

Simulation results are first presented for the largest wind estimation error, that of Type A wind errors. Results were compiled from 54 separate simulations, each considering controlled/uncontrolled releases from

21-43 locations. In total, 1009 individual descent paths were computed for each of the controlled and uncontrolled descent vehicles. Identical wind data was used for each individual controlled/uncontrolled comparision. For the numerous wind data sets considered, spatial differences varied between $0 - 153km$ and temporal differences varied between $63 - 217min$. With the Type A (large) wind errors, the calculated error probable (CEP) was found to be $3083m$ and $1811m$ for the uncontrolled and controlled descent vehicles, respectively. Paired, two-sided t-tests were performed the simulation results to quantify the effectiveness of the controlled vehicles in comparision with the uncontrolled vehicles. In the 38 completed simulations, the t-test failed seven times (at a 95% confidence level), with an average p value of 4.45×10^{-2}. I.e., the landing locations were statistically different in 31 of the 38 cases studied. Landing locations for a typical simulation with Type A wind errors are shown in Figure 9. Typical wind data used for the Type A wind error simulations are shown in Figure 10.
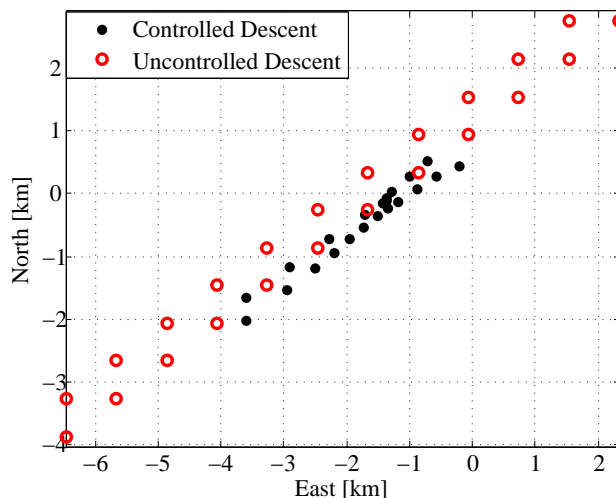

Figure 9. Landing locations of uncontrolled and controlled parachute vehicles for a typical descent simulation using Type A wind estimation errors. The release locations for these simulations are shown in Figure 8.
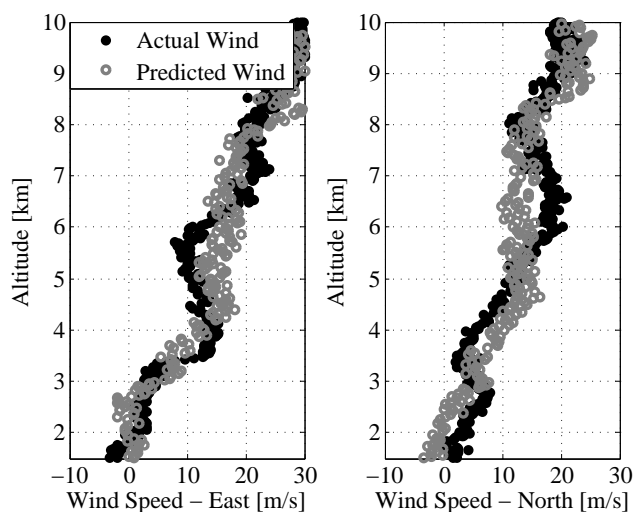

Figure 10. Wind profiles used for predicted and actual wind profiles for a typical Type A simulation.

Results were compiled for seven separate simulations for the transition-type wind estimation errors. These results were computed by comparing the dropsonde-descent-recorded winds with other dropsonde descents. These dropsondes varied in time (up to 9 minute difference in release time) and location (up to $4.1km$ difference in release location). The CEP was found to be $2614m$ and $893.2m$ for the uncontrolled and

American Institute of Aeronautics and Astronautics

controlled descent vehicles, respectively. The t-test did not fail for any simulations, with an average p value of 5.45×10^{-7}. Landing locations for a typical simulation with the transition type wind errors is shown in Figure 11. Typical wind data used for the Transition wind error simulations are shown in Figure 12.
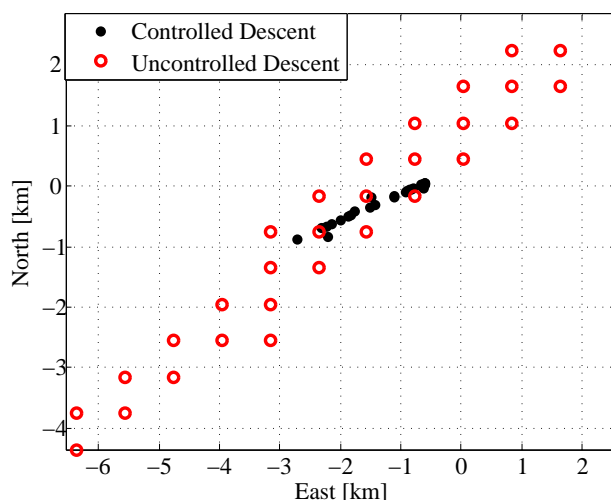

Figure 11. Landing locations of uncontrolled and controlled parachute vehicles for a typical simulation containing wind estimation errors in the Transition regime between Types A and B.
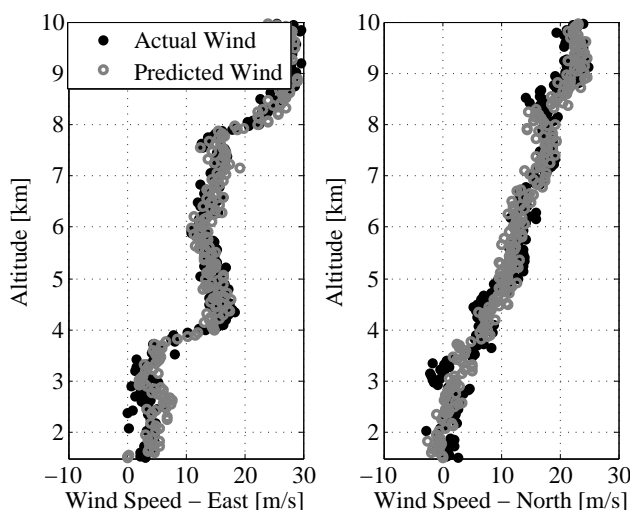
Figure 12. Wind profiles used for predicted and actual wind profiles for a typical simulation containing wind estimation errors in the Transition regime between Types A and B. Note the better agreement between predicted and actual winds in comparison with Type A wind errors (Figure 10).

For Type B wind estimation errors, nine separate simulations were conducted. These simulations were computed by comparing the balloon-recorded winds for the seven different balloons launched (at two separate times). As discussed previously, the ascent rates were nearly matched with discrepancies between average ascent rates of approximately $0.15m/s$. The CEP was found to be $2740m$ and $295.1m$ for the uncontrolled and controlled descent vehicles, respectively. The t-test again did not fail for any simulation, with the average p value of 2.86×10^{-7}. Landing locations for a typical simulation with Type B wind errors are shown in Figure 13, resulting from winds such as those in Figure 14 (typical).
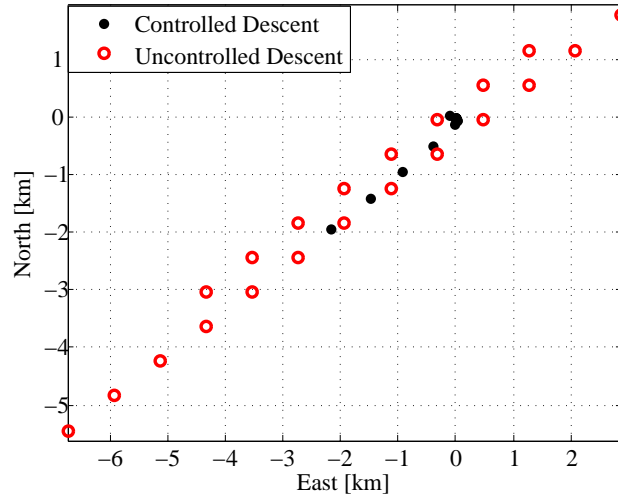
American Institute of Aeronautics and Astronautics

Figure 13. Landing locations of uncontrolled and controlled parachute vehicles for a typical simulation containing wind estimation errors of Type B.
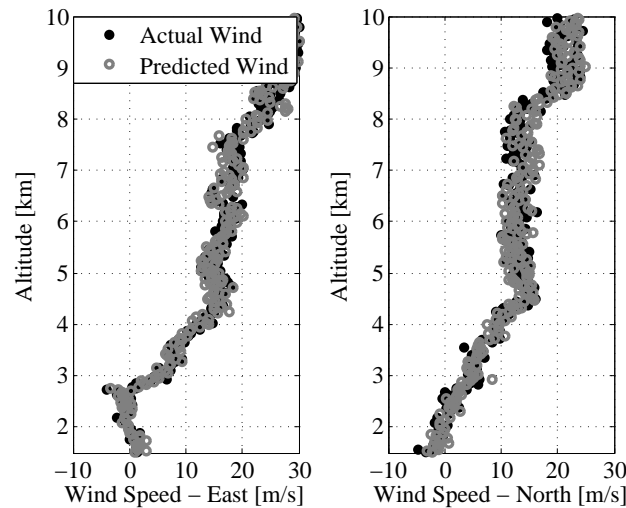

Figure 14. Wind profiles used for predicted and actual wind profiles for a typical simulation containing wind estimation errors of Type B. Again, note the better agreement between predicted and actual winds in comparison with Type A wind errors (Figure 10).

VII. Discussion

Although the methodology developed does not produce pin-point accuracy (such as a parafoil), it can provide greatly-improved accuracy over uncontrolled circular parachute descents, provided good wind data are available. However, with inaccurate wind information, the trajectory planning results in large errors in landing location, and in these cases, the controlled descent vehicle provides only a small improvement in accuracy. As wind estimation becomes more accurate, the accuracy of the descent vehicle greatly improves. These simulations demonstrate the potential for a circular parachute to overcome release location errors. By performing high-altitude, high-opening parachute drops, the descent vehicle has a relatively large performance envelope. The typical performance envelope provides more than enough release location error rejection, as many envelopes are $11km$ in length along the major axis. Even at lower release altitudes, the performance envelope provides adequate size to capture reasonable release location errors. For example, with a release altitude of $3km$ AGL, the typical performance envelope will have a major axis length of $2.5km$ (depending on wind conditions).

American Institute of Aeronautics and Astronautics

In all of the simulations, some controlled descent paths end up significantly farther away from the target, when compared to the other controlled descent paths. This is because the path planning algorithm uses the predicted winds to create the predicted performance envelope. In reality, the actual performance envelope will differ from the predicted one. This can cause decisions based solely on the predicted envelope to further push the vehicle outside of the actual envelope. The actual envelope can not be known *a priori*. For this reason, it is beneficial to release as near to the center of the envelope as possible, thereby providing maximum rejection of inaccurate wind data effects.

The simulations show statistically-significant improvements in performance for descent rate controlled parachutes in comparison with uncontrolled parachutes. Results from the t-tests further confirm the notion that the vehicle does indeed alter the landing location. For both Type B and Transition wind types, the t-tests performed concluded that with an extremely high confidence level, the landing locations for the paired uncontrolled and controlled landing locations are statistically different (improved in all cases). Even for the less accurate Type A wind errors, the controlled descent vehicle did improve the landing location the majority of the time (36 of 38 simulations); however, the only 32 of the 38 controlled descent simulations were statistically different than the uncontrolled counterparts.

In practice, the descent rate control method will also automatically overcome any vehicle uncertainties (parachute/payload mass and drag area) as well as release location errors, because the system attempts to reach a desired descent speed. If the payload mass is larger than initially estimated, for example, the parachute's controllable descent speed range will be shifted with higher descent speeds for both the maximum and minimum parachute drag areas. As long as the desired descent velocity is not out of this range, the vehicle will simply reef until the desired descent speed has been reached.

VIII.   Conclusions

A technique was developed to utilize winds aloft to manipulate the landing location of a parachute through the use of descent rate control. By adjusting the drag area of the parachute continuously, the landing location can be controlled. Using a 3–DOF model to predict the descent path, an efficient algorithm adjusts the descent rate at regular altitude intervals to provide the most robust path by traveling towards the center of the performance envelope. The control system has only one output, although this output changes in time, thus providing both longitudinal and latitudinal control in an air column where wind direction varies with altitude.

The simulation results presented here show the extent to which accurate foreknowledge of the wind is crucial for effective guidance. For the best results, wind data should be collected in the immediate vicinity and as close to the release time as possible. In such scenarios, the descent vehicle is capable of overcoming both release location errors, as well as vehicle uncertainties (thereby causing descent speed errors). The methodology developed provides a new technique for utilizing circular parachutes to accurately control the landing location in high-altitude release scenarios. It should be noted that the significant performance improvements demonstrated here were for a comparatively-simple situation using a circular parachute. The performance envelope construction scheme developed here can also readily be integrated into more complex descent vehicle systems (such as guided parafoils) to provide an additional robust path-planning tool that takes advantage of available wind data to potentially expand the performance envelope and as an additional mechanism for control during a guided descent.

Acknowledgements

American Institute of Aeronautics and Astronautics

References

[1]Yakimenko, O. A., Dobrokhodov, V. N., and Kaminer, I. I., "Synthesis of Optimal Control and Flight Testing of an Autonomous Circular Parachute," *Journal of Guidance, Control, and Dynamics*, Vol. 27, No. 1, 2004, pp. 29–40.

[2]Brown, G., Haggard, R., Almassy, R., Benney, R., and Dellicker, S., "The Affordable Guided Airdrop System (AGAS)," *15th AIAA Aerodynamic Decelerator Systems Technology Conference and Seminar*, June 8-11, 1999, Toulouse, France.

[3]Dellicker, S. H. and Bybee, J., "Low Cost Parachute Guidance, Navigation, and Control," *AIAA 15th Aerodynamic Decelerator Systems Conference*, 8-11 June 1999, Toulouse, France, AIAA-99-1706.

[4]Gilles, B., Hickey, M., and Krainski, W., "Flight Testing of a Low-Cost Precision Aerial Delivery System," *18th AIAA Aerodynamic Decelerator Systems Technology Conference and Seminar*, May 23-26, 2005, Munich, Germany.

[5]Jorgensen, D. S. and Hickey, M. P., "The AGAS 2000 Precision Airdrop System," *Proceedings of Infotech@Aerospace*, Arlington, Virginia, September 26-29, 2005.

[6]Slegers, N. and Costello, M., "Aspects of Control for a Parafoil and Payload System," *Journal of Guidance, Control, and Dynamics*, Vol. 26, No. 6, 2003, pp. 898–905.

[7]Yakimenko, O., "On the Development of a Scalable 8-DoF Model for a Generic Parafoil-Payload Delivery System," *18th AIAA Aerodynamic Decelerator Systems Technology Conference and Seminar*, May 23-26, 2005, Munich, Germany.

[8]Slegers, N., "Effects of Canopy-Payload Relative Motion on Control of Autonomous Parafoils," *Journal of Guidance, Control, and Dynamics*, Vol. 33, No. 1, 2010, pp. 116–125.

[9]Slegers, N., Beyer, E., and Costello, M., "Use of Variable Incidence Angle for Glide Slope Control of Autonomous Parafoils," *Journal of Guidance, Control and Dynamics*, Vol. 31, No. 3, 2008, pp. 585–596.

[10]Benney, R., Barber, J., McGrath, J., McHugh, J., Noetscher, G., and Tavan, S., "The Joint Precision Airdrop System Advanced Concept Technology Demonstration," *18th AIAA Aerodynamic Decelerator Systems Technology Conference and Seminar*, Munich, Germany, AIAA 2005-1601, May 2005.

[11]Hattis, P., Angermueller, K., Fil, T., Wright, R., Benney, R., and LeMoine, D., "An In-Flight precision Airdrop Planning System," *23rd Army Science Conference*, Orlando, Florida, December 2-5, 2002.

[12]Fields, T. D., LaCombe, J. C., and Wang, E. L., "Autonomous Guidance of a Circular Parachute Using Descent Rate Control," *Journal of Guidance, Control, and Dynamics*, Vol. 35, No. 4, 2012, pp. 1367–1370.

[13]Braun, R. and Manning, R., "Mars exploration entry, descent and landing challenges," *Aerospace Conference, 2006 IEEE*, 0-0 2006, p. 18 pp.

[14]Kelly, K. and Pena, B., "Wind Study and GPS Dropsonde Applicability to Airdrop Testing," *16th AIAA Aerodynamic Decelerator Systems Technology Conference and Seminar*, 21-24 May, 2001, Boston, MA.

[15]Benjamin, S. S., Jamison, B. D., Moninger, W. R., Schwartz, B., and Schlatter, T. W., "Relative forecast impact form aircraft, profiler, rawinsonde, VAD, GPS–PW, METAR and mesonet observations for hourly assimilation in the RUC," *12th Conference on IOAS-AOLS, American Meteorological Society*, 20-24 January 2008, New Orleans, LA.

[16]Hock, T. F. and Franklin, J. L., "The NCAR GPS Dropwindsonde," *Bulletin of the American Meteorological Society*, Vol. 80, No. 3, 1999, pp. 407–420.

[17]Chen, J.-S., Hassenpflug, G., and Yamamoto, M., "Tilted refractive-index layers possibly caused by KelvinHelmholtz instability and their effects on the mean vertical wind observed with multiple-receiver and multiple-frequency imaging techniques," *Radio Science*, Vol. 43, 2008.

[18]Bertin, J. J. and Cummings, R. M., *Aerodynamics for Engineers*, Vol. 1, chap. 1, Prentice Hall, Upper Saddle River, New Jersey, 5th ed., 2009, pp. 15–17.

American Institute of Aeronautics and Astronautics